Reports

Epitaxial and Smooth Films of *a*-Axis $YBa_2Cu_3O_7$

C. B. EOM,* A. F. MARSHALL, S. S. LADERMAN, R. D. JACOWITZ, T. H. GEBALLE

$YBa_2Cu_3O_7$ films have been grown epitaxially on $SrTiO_3$ (100) and $LaAlO_3$ (100) substrates with nearly pure *a*-axis orientation and with transition temperature T_c ($R = 0$) of 85 K. A unique feature of these films is their smooth surface. These smooth surfaces enable the growth of short-period superlattices with well-defined modulations. The films are untwinned and the grains grow with their *c*-axis along one of two perpendicular directions on the substrate ([100] or [010]). The fabrication of sandwich-type Josephson junctions with good characteristics may now be possible because unlike *c*-axis–oriented films, the superconducting coherence length of these smooth films is appreciably large perpendicular to their surfaces.

THE INHERENTLY HIGHLY ANISOTROPIC nature of the electrical properties of all the high transition temperature (T_c) superconductors is known to derive from their structure. Electrical transport is concentrated along the copper oxygen planes, and as a result the electrical conductivity parallel to the conducting planes is measured to be from two to five orders of magnitude greater than in the *c*-direction for well-made samples of $YBa_2Cu_3O_7$ (YBCO) (*1*) and $Bi_2Ca_2SrCu_2O_8$. The perpendicular conductivity in even the best single crystals and films can be masked by defects such as stacking faults, but it seems to be well below the limit for minimum metallic conductivity (*2*). The large anisotropy persists in the superconducting state where, for example, the superconducting coherence length is about 2 Å along the *c*-axis but 10 Å or more along the *ab*-planes (*3*). In the present work the growth of high-quality films with the *a*-axis normal to the film surface is described. These films offer new opportunities for studying properties in the purely *a*-direction.

Up to the present, the highest quality epitaxial films of high T_c superconductors have been grown only in the *c*-axis orientation with the conducting *ab* planes parallel to the substrate. Such films have in-plane electrical properties comparable to the best single crystals. Unfortunately it has not been possible to make sandwich tunnel junctions with the *c*-axis films as the base electrode. This frustrates attempts to investigate superconductivity by tunnelling spectroscopy and to obtain well-behaved Josephson junctions needed for technological applications. It is well accepted that the problems arise because of the extremely short superconducting coherence lengths in the *c*-direction. Tunneling probes roughly only 2 Å and as a result the bulk superconductivity must be maintained right up through the surface layer. Any change in the composition of the surface will degrade the superconductivity and the tunneling behavior. The larger coherence length in the *ab* plane makes it attractive to consider junctions in other orientations.

Convincing evidence for the above statements was obtained recently (*4*, *5*) by studying superconducting-normal-superconducting (SNS') junctions. In the work of Lee *et al.* (*5*) the junctions were made by depositing gold and then lead on smooth YBCO films which were oriented about 70% *a*-axis and 30% *c*-axis. The junction areas were small enough so that statistically a substantial fraction of the junctions could be expected to be purely *a*-axis. Roughly half of the junctions had large Josephson currents whereas the others, like the junctions on purely *c*-axis films, had no Josephson currents at all. As a result we have concentrated on growing purely *a*-axis films. In the present work conditions for reproducibly obtaining *a*-axis films have been established. X-ray diffraction analyses show less than 0.1 volume percent of other orientations. As a further unexpected and very fortunate result the films are atomically smooth and thus attractive candidates for making tunnel junctions in a sandwich configuration.

Previously it has been found possible to grow predominantly (that is, ~99%) *a*-axis films from slightly Cu- and Y-rich compositions with thicknesses >3000 Å by post-deposition annealing at low temperature (*6*). These films have extremely rough surfaces. These *a*-axis films also tend to have *c*-axis texture near the substrate; the degree of *a*-axis texture increases with increasing film thickness. We also reported in situ growth

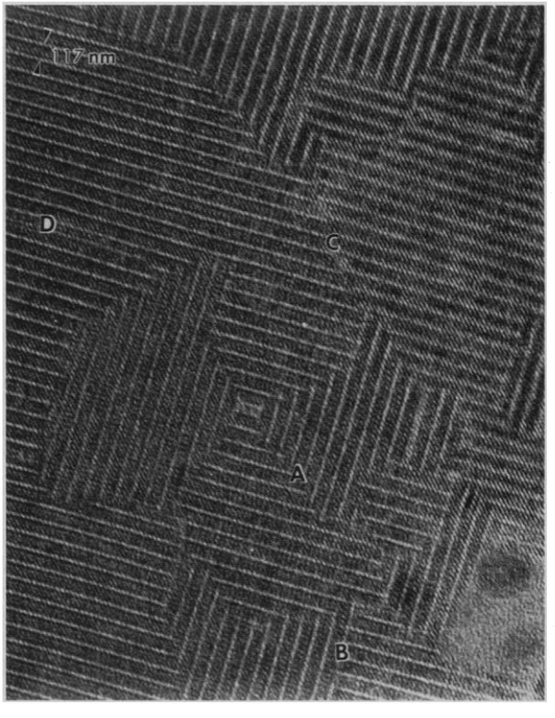

Fig. 1. Planar transmission electron micrograph of an *a*-axis film. Small *a*-axis grains and various grain boundaries (A, B, C, and D) are shown.

C. B. Eom and T. H. Geballe, Department of Applied Physics, Stanford University, Stanford, CA 94305.
A. F. Marshall, Center for Materials Research, Stanford University, Stanford, CA 94305.
S. S. Laderman and R. D. Jacowitz, Hewlett-Packard, Palo Alto, CA 94304.

*Also at the Center for Materials Research, Stanford University, Stanford, CA 94305.

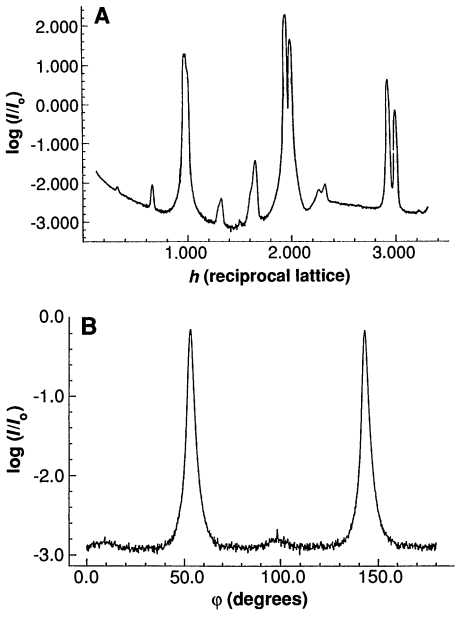

Fig. 2. X-ray diffraction scans of an *a*-axis film. (**A**) Radial scan along *a*-axis–oriented YBCO *a** direction. (**B**) Azimuthal scan of the (102) reflection from *a*-axis grains.

Table 1. The properties of YBCO films grown under the different conditions. Films on $SrTiO_3$ (100) and $LaAlO_3$ (100) substrates grown at low temperture show *a*-axis texture.

Substrate	T_s (°C)	Textures	T_c (K)	ΔT_c (K)	*a*-lattice parameter (Å)	ρ(0) (μohm-cm)	dρ/dT (μohm-cm/K)	J_c (4.2 K) (A/cm^2)
$SrTiO_3$ (100)	640	*a*	85	3	3.81	800	1.1	1×10^6
$LaAlO_3$ (100)	640	*a*	84	3	3.81	900	1.5	1×10^6
MgO (100)	640	*c*	85	<1	—	40	0.7	3×10^7
YSZ (100)	640	*c*	84	<1	—	—	—	2×10^7
Al_2O_3 ($1\bar{1}02$)	640	70%*c* + 30%*a*	—	—	—	—	—	—
$SrTiO_3$ (100)	720	*c*	86.5	<1	—	0	0.6	5×10^7
MgO (100)	720	*c*	86.5	<1	—	0	0.6	5×10^7

of nearly pure *a*-axis films by single target sputtering but the surfaces of these films were not smooth (7). At the same time, quite pure *a*-axis films of $EuBa_2Cu_3O_7$ made in situ by magnetron sputtering were reported by Asano *et al.* (*8*). Their scanning electron microscope (SEM) analysis revealed fairly uniform surfaces. Those authors also reported they were unable to make high-quality *a*-axis films of $YBa_2Cu_3O_7$. The highest quality in situ grown films up to the present work have had *c*-axis structures.

By using the high-pressure single target 90° off-axis sputtering technique (*7, 9*) we have been able to grow very smooth and pure *a*-axis films in situ on $SrTiO_3$ (100) or $LaAlO_3$ (100) substrates under the condition given in Table 1. The sputtering atmosphere consisted of 40-mTorr O_2 and 60-mTorr Ar. The rf-power (125 W) on the sputter gun generated a self-bias of 50 V. The substrate block temperature T_s was held at 640°C. Films grown under similar conditions on MgO (100), YSZ (100), or Al_2O_3 ($1\bar{1}02$) substrates have predominantly *c*-axis textures. However, the films grown on $SrTiO_3$ buffer-layered MgO (100) have *a*-axis texture. We believe the different textures on the different substrates may be due to a competition between minimizing the surface energy of the film (which favors *c*-axis orientation as evident in the morphology of single crystals) and minimizing energy as a result of structural coherence at the film/substrate interface during the early stage of growth. Both $SrTiO_3$ and $LaAlO_3$ have a perovskite structure similar to YBCO, and the lattice matching between these substrates and YBCO is also quite good. Evidently at the relatively low growth temperatures (Table 1), the reduced surface mobility and the possibility of film/substrate coherency leads to the formation of *a*-axis films. At higher substrate temperatures *c*-axis growth dominates because the species mobility is sufficiently high to permit the minimization of surface energy. In the case of the other substrates (MgO, YSZ, and Al_2O_3), the lattice mismatch with YBCO is large and there is less persistence of structural coherency at the film/substrate interface as the films grow. The films apparently grow so as to minimize their surface energies resulting in incoherent *c*-axis texture.

Figure 1 shows a planar view transmission electron micrograph of a typical *a*-axis film. Lattice fringes perpendicular to the *c*-axis are clearly seen in the *a*-axis–oriented grains. The *a*-axis–oriented YBCO grains are seen to be 100 to 500 Å wide. The predominant *a*-axis grains lie along one of two orthogonal directions, with their *c*-axes along the substrate [100] or [010]. Boundaries between and within *a*-axis grains are apparent. In large area micrographs, the most prevalent boundary type is as indicated by "A" in Fig. 1. The *ab*-planes meet at 90° along a 45° boundary covering nearly the entire width of the grain. These boundaries appear responsible for the connected dc current transport paths described below. Occasionally, grains meet along a boundary parallel to one grain's *ab*-planes, as indicated by "B" in Fig. 1. Simple models would predict these boundaries stop dc current more effectively than boundaries of type "A." Planar boundaries between regions with the same epitaxial orientation are also visible in the micrograph. Boundaries of "C" and "D" are antiphase-type boundaries lying obliquely and perpendicular to the *c*-axis, respectively. Boundaries of type "D" would appear to have little effect on intragrain current transport along the *ab*-plane.

The relative volume fractions of epitaxial material and the phase purity of the films were investigated with x-ray diffraction. Figure 2A shows an x-ray diffraction scan along the *a** (reciprocal lattice vector) direction of the *a*-axis–oriented YBCO. The strongest reflections correspond to the substrate and film (100), (200), and (300) reflections. The high degree of perpendicular alignment of the YBCO *a*-axis grains is confirmed by the 0.2 degree FWHM of a rocking curve scan of the (200) peak. In Fig. 2, very weak peaks appear at positions close to, but clearly different from those expected for *c*-axis–oriented YBCO. Their positions and breadths are consistent with faulted layered material, much like faulted YBCO but with an average *c*-lattice parameter close to 11.57 Å. This interpretation implies a volume fraction of *a*-axis aligned YBCO about 99.9 volume percent, consistent with observations by transmission electron microscopy.

Figure 2B shows the dependence of x-ray intensity corresponding to the YBCO (102) reflection as a function of azimuthal angle. The main peaks correspond to the epitaxial arrangements YBCO[001]/$SrTiO_3$[100] and YBCO[001]/$SrTiO_3$[010]. Close to 99.9 volume percent of the *a*-axis grains lie along these directions.

The x-ray data of Fig. 2B were supplemented with grazing incidence geometry scans of (005), (007), (027), and (032) type reflections of the *a*-axis grains to determine their *b*- and *c*-lattice parameters. We find a_0 = 3.81 Å, b_0 = 3.89 Å, and c_0 = 11.72 Å. As with *c*-axis–oriented in situ grown YBCO thin films, the lattice parameters are different from those found in bulk, fully oxygenated YBCO (7). In the bulk case, a_0 = 3.82 Å, b_0 = 3.89 Å, and c_0 = 11.68 Å (*10*). A portion of the difference between the parameters for the film and for bulk YBCO could be a result of elastic strains related to differences in thermal expansion coefficients and the process of oxygenating the YBCO at low temperatures. We note that the *c*-axis lattice parameter observed here is typical of those found for *c*-axis–aligned films and that there it is clear that the expansion is not entirely due to biaxial thermal expansion, lattice mismatch–induced strain, or simple

oxygen deficiency (*11, 12*). We suspect that atomic disorder, relative to bulk YBCO, is responsible for a major portion of the difference in *c*-lattice parameters, and possibly the lowered T_c as well.

Because at the growth temperature YBCO is tetragonal (no distinction between *a* and *b*), whether the *a*-axis or the *b*-axis is perpendicular to the surface is determined while cooling from the growth temperature. To avoid overlapping substrate reflections, the possibility that YBCO grains with their *b*-axis perpendicular to the surface exists in these films was checked by x-ray diffraction with the scattering vector perpendicular to the surface for films on $LaAlO_3$ and in grazing incidence geometry for films on $SrTiO_3$. No evidence of *b*-axis grains was found. The *a*-axis films are twin free, in contrast to *c*-axis–oriented films.

The surface morphology of these pure *a*-axis films was investigated by scanning electron microscopy (SEM). The surface of the 2000 Å thick *a*-axis films under SEM was found to be featureless with a lateral resolution limit of 100 Å. The films were further examined with a scanning force microscope (SFM) (*13*) (Fig. 3). With this instrument, a maximum feature height of only 40 Å was resolved over the entire 16-μm^2 area studied. Along any 4-μm linear scan, only about ten modulations were observed. This is roughly equivalent on the average to one layer over 50 unit cells, suggesting that these films are atomically smooth over large areas.

Transition temperatures and normal state resistivities were measured by a four-point dc transport method using a 400-μm-wide line, 2 mm long, patterned bridge. The bridge lay along the substrate [100]. Figure 4 shows the resistivity versus temperature curves of a pure *a*-axis film on $SrTiO_3$ (100) and a pure *c*-axis film on MgO (100) grown under the same conditions and a *c*-axis film on MgO grown at a higher temperature. The transition widths of the *a*-axis and *c*-axis films are 3 K and 0.5 K, respectively.

The *a*-axis orientation strongly modifies current transport in the plane of the film compared to *c*-axis–aligned films. Macroscopically, current flows along the substrate [100] in these experiments. While it is not always the case, the normal state resistivities of in situ *a*- as well as *c*-axis films are most frequently linear with temperature as are the examples shown here. Both the slopes of $\rho_N(T)$ and the extrapolated intercept at $T = 0$ differ among these samples.

The largest systematic difference between the *a*-axis and *c*-axis films is the much larger zero-temperature intercept for the extrapolated normal state resistivity [ρ(0)] in the *a*-axis case. In general, differences in $\rho(T)$ may be due to lengthening or area reduction of the current paths, increases in intragrain elastic scattering, or increases in grain boundary resistances (*14*).

We expect that microscopically the currents flow predominantly along the *ab*-planes in the *a*-axis films, sometimes along the macroscopic current path and sometimes perpendicular. Such paths along the *ab*-plane are easily visualized with reference to Fig. 1. Thus path lengthening and related percolative effects are expected for the *a*-axis films. However, such geometrical effects will raise the slope ($d\rho/dT$) as well as the intercept in the same proportion. The data show that the slope tends to rise, but no more than a factor of three for the *a*-axis films compared to the *c*-axis films. The ρ(0) increases much more than this.

Differences in intragrain elastic scattering between *a*-axis and *c*-axis films are possible, especially when comparing *c*-axis films grown at high temperatures to *a*-axis films grown at lower temperatures. To see how large such effects may be, *c*-axis–oriented films grown at two different temperature are compared in Fig. 4 and Table 1. An increase in scattering is evident for the film having the lower deposition temperature. This difference has intragrain and grain boundary contributions. The observed difference sets an upper bound estimate for the intragrain scattering increase. It is likely that for a fixed deposition temperature, the intragrain component along the *ab*-plane is nearly independent of grain orientation. Such a component thus seems too small to account for the large ρ(0) seen in the *a*-axis case.

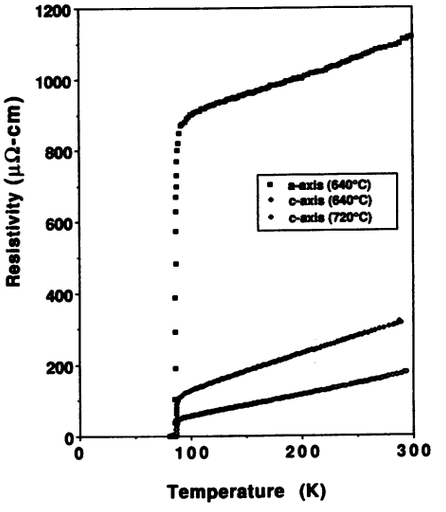

Fig. 4. Resistivity versus temperature curves of a *c*-axis film grown at 720°C on MgO, a *c*-axis film grown at 640°C on MgO, and an *a*-axis film grown at 640°C on $SrTiO_3$.

The large ρ(0) for the *a*-axis case then is seen to be associated with grain boundary scattering. The high density of boundaries seen in Fig. 1 make plausible their strong contribution to carrier scattering. In fact, the resistance per boundary implied by this interpretation of our data is of the same order as boundary resistances observed for high-angle grain boundaries (*15*). As seen next, they also likely dominate the critical current behavior.

The critical current densities of the *a*-axis films were measured using a dc magnetization method, making use of the Bean (*16*) approximation and confirmed by transport. The critical current J_c at 4.2 K at zero field was about 1×10^6 A/cm^2. This value is low compared to the *c*-axis films (6×10^7 A/cm^2) (*7*) and similar in magnitude to thin films having other orientations such as (103) and (113) (*19*). These data suggest the critical current is limited by various grain boundaries (*17*) shown in the transmission electron micrograph. At these densities, such grain boundaries may be useful for making multiarray weak-link devices.

In conclusion, it has been demonstrated

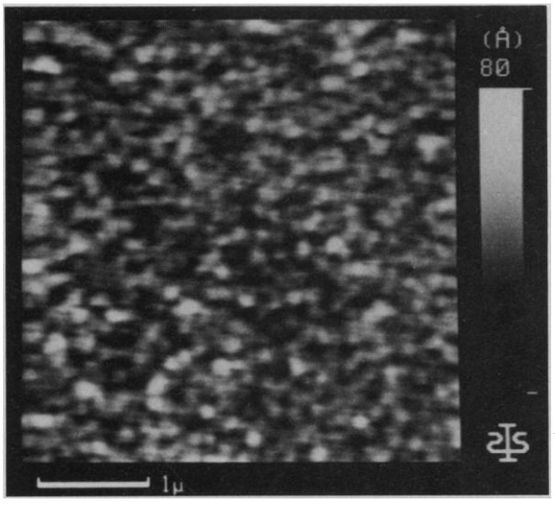

Fig. 3. Surface morphology of the pure *a*-axis film under the scanning force microscope. No features were observed by scanning electron microscopy with a lateral resolution of 100 Å.

that high quality, pure, and atomically smooth *a*-axis films can be grown in situ. The single target 90° off-axis sputtering technique used maintains the surface quality over macroscopic areas and makes fabricating high T_c sandwich-type junctions possible. In fact, we have already prepared *a*-axis superlattices with $PrBa_2Cu_3O_7$ which show well-defined periods as low as 24 Å (*18, 19*). It should be possible to study transport in ribbons which are only 12 Å or less.

REFERENCES AND NOTES

1. S. W. Tozer *et al.*, *Phys. Rev. Lett.* **59**, 1768 (1987).
2. N. F. Mott, *Philos. Mag.* **22**, 7 (1970).
3. B. Oh *et al.*, *Phys. Rev. B* **37**, 7861 (1988).
4. H. Akoh, C. Camerlingo, S. Takada, *Appl. Phys. Lett.* **56**, 1487 (1990).
5. M. Lee *et al.*, in preparation.
6. K. Char *et al.*, *IEEE Trans. Magnetics* **25**, 2422 (1989).
7. C. B. Eom *et al.*, *Appl. Phys. Lett.* **55**, 595 (1989).
8. H. Asano *et al.*, *Jpn. J. App. Phys.* **28**, L981 (1989).
9. C. B. Eom *et al.*, *Physica C*, in press.
10. R. J. Cava *et al.*, *Phys. Rev. Lett.* **58**, 1676 (1987).
11. W. R. McKinnon *et al.*, *Phys. Rev. B* **38**, 6543 (1988).
12. R. J. Cava *et al.*, *Physica C* **153–155**, 560 (1988).
13. Data were taken on a Parks Scientific Instrument Model SFM-BD2 scanning force microscope.
14. J. Halbritter, *Intl. J. Mod. Phys. B* **3**, 719 (1989).
15. S. E. Russek *et al.*, *Appl. Phys. Lett.*, in press.
16. C. P. Bean, *Phys. Rev. Lett.* **54**, 1702 (1962).
17. D. Dimos, P. Chaudhari, J. Mannhart, F. K. LeGoues, *Phys. Rev. Lett.* **61**, 219 (1988).
18. C. B. Eom and T. H. Geballe, paper presented at 1990 MRS Spring Meeting (San Francisco, 20 April 1990), Symposium M.
19. C. B. Eom *et al.*, in preparation.

20. We thank M. D. Kirk and R. S. Howland for the SFM image of the *a*-axis film surface and J. Halbritter for helpful discussions. This work has been supported by AFOSR under contract F49620-88-C-004, by the Center for Research in Superconductivity and Superconducting Electronics under contract F49620-88-C-001 and by the Stanford Center for Materials Research under the NSFMRL program.

20 July 1990; accepted 14 August 1990

Direct Interaction of a Ligand for the *erb*B2 Oncogene Product with the EGF Receptor and p185^{erbB2}

RUTH LUPU,* RAMON COLOMER, GERHARD ZUGMAIER, JAY SARUP, MICHAEL SHEPARD, DENNIS SLAMON, MARC E. LIPPMAN

The *erb*B2 oncogene encodes a 185-kilodalton transmembrane protein whose sequence is similar to the epidermal growth factor receptor (EGFR). A 30-kilodalton factor (gp30) secreted from MDA-MB-231 human breast cancer cells was shown to be a ligand for p185^{erbB2}. An antibody to EGFR abolished the tyrosine phosphorylation induced by EGF and transforming growth factor–α (TGF-α) but only partially blocked that produced by gp30 in SK-BR-3 breast cancer cells. In two cell lines that overexpress *erb*B2 but do not express EGFR (MDA-MB-453 breast cancer cells and a Chinese hamster ovary cell line that had been transfected with *erb*B2), phosphorylation of p185^{erbB2} was induced only by gp30. The gp30 specifically inhibited the growth of cells that overexpressed p185^{erbB2}. An antibody to EGFR had no effect on the inhibition of SK-BR-3 cell colony formation obtained with gp30. Thus, it appeared that gp30 interacted directly with the EGFR and *erb*B2. Direct binding of gp30 to p185^{erbB2} was confirmed by binding competition experiments, where gp30 was found to displace the p185^{erbB2} binding of a specific antibody to p185^{erbB2}. The evidence described here suggests that gp30 is a ligand for p185^{erbB2}.

THE HUMAN C-*erb*B2 ONCOGENE encodes a 185-kD transmembrane glycoprotein with tyrosine kinase activity. This protein, p185^{erbB2}, shows extensive structural similarity with the p170 EGFR and is thought to be a growth factor receptor (*1–4*). No ligand for p185^{erbB2} has as yet been fully characterized. EGF and TGF-α, the normal ligands for the EGFR, do not interact directly with p185^{erbB2} (*5, 6*). Amplification of *erb*B2 occurs in many adenocarcinomas and it is overexpressed in nearly 30% of human breast cancer patients (*7–9*). In addition, p185^{erbB2} is necessary for the maintenance of the malignant phenotype of cells transformed by *erb*B2 (*10*).

We have previously identified and purified a growth factor that is secreted by MDA-MB-231 human breast cancer cells (*11*). This 30-kD glycoprotein (gp30) is similar to TGF-α in its ability to bind to the EGFR, phosphorylate EGFR, and induce NRK colony formation. However, it is distinct from the 18-kD precursor for TGF-α and 6-kD mature TGF-α, as shown by peptide mapping of the translated proteins (*11*). The purification profile of the preparation of the 30-kD polypeptide used in the current studies is shown in Fig. 1.

To characterize the cellular effects of gp30, we assessed its ability to induce tyrosine phosphorylation in human breast cancer cell lines MDA-MB-468 and SK-BR-3. The *EGFR* gene is amplified and overexpressed in MDA-MB-468 cells (*7*), although they do not express detectable concentrations of *erb*B2. Amplification and overexpression of the *erb*B2 gene occur in SK-BR-3 cells, and they also have moderately elevated concentrations of the EGFR (*12*). TGF-α, gp30 (Fig. 2), and EGF induced tyrosine phosphorylation in both cell lines. An antibody against the EGFR (anti-EGFR) abolished the phosphorylation induced by the three growth factors in MDA-MB-468 cells. However, this antibody did not completely block the phosphorylation induced by gp30 in SK-BR-3 cells, although in these cells it blocked the phosphorylation induced by TGF-α (Fig. 2). This result suggested that tyrosine phosphorylation of a protein different from the EGFR occurred in gp30-treated SK-BR-3 cells. No phosphorylation was observed in untreated SK-BR-3 cells or cells treated only with the antibody to EGFR (Fig. 2).

To test whether this tyrosine phosphorylated protein was p185^{erbB2}, we used the human mammary carcinoma cell line MDA-MB-453 (*12*), which overexpresses *erb*B2 but has undetectable concentrations of the EGF receptor protein or mRNA (*13*). In these cells, gp30 induced a significant increase in tyrosine phosphorylation in a dose-dependent manner (Fig. 3).

To further analyze the effects of gp30, we studied Chinese hamster ovary (CHO) cells transfected with human *erb*B2 (CHO/*erb*B2) (*14, 15*). Induction of p185^{erbB2} phosphorylation was detected in gp30-treated CHO/*erb*B2 cells with an antibody to phosphotyrosine (Fig. 4). No tyrosine phosphorylation was observed in control CHO cells transfected with the gene for dihydrofolate reductase (DHFR) (CHO/DHFR) or in untreated cells. Levels of p185^{erbB2} did not change after treatment with gp30 in CHO/*erb*B2 cells (Fig. 4).

In summary, in all the cell lines described above, EGF and TGF-α were unable to induce p185^{erbB2} phosphorylation. No phosphorylation was observed in untreated cells. This supported the hypothesis of an apparently direct interaction between gp30 and p185^{erbB2}

We next examined the effects of gp30 on

R. Lupu, R. Colomer, G. Zugmaier, M. E. Lippman, The Vincent T. Lombardi Cancer Research Center, Georgetown University Medical Center, 3800 Reservoir Road, Washington, DC 20007.
J. Sarup and M. Shepard, Genentech, San Francisco, CA 94080.
D. Slamon, Division of Hematology-Oncology, Department of Medicine, UCLA, Los Angeles, CA 90024.

*To whom correspondence should be addressed.